

ACS APPLIED MATERIALS & INTERFACES

Subscriber access provided by University Libraries | Virginia Tech & VIVA (Virtual Library of Virginia)

Applications of Polymer, Composite, and Coating Materials

Quadruple Hydrogen Bonding Supramolecular Elastomers for Melt Extrusion Additive Manufacturing

Xi Chen, Callie Zawaski, Glenn A Spiering, Boer Liu, Christina M Orsino, Robert B. Moore, Christopher Bryant Williams, and Timothy E. Long

ACS Appl. Mater. Interfaces, Just Accepted Manuscript • DOI: 10.1021/acsami.0c08958 • Publication Date (Web): 10 Jun 2020

Downloaded from pubs.acs.org on June 23, 2020

Just Accepted

"Just Accepted" manuscripts have been peer-reviewed and accepted for publication. They are posted online prior to technical editing, formatting for publication and author proofing. The American Chemical Society provides "Just Accepted" as a service to the research community to expedite the dissemination of scientific material as soon as possible after acceptance. "Just Accepted" manuscripts appear in full in PDF format accompanied by an HTML abstract. "Just Accepted" manuscripts have been fully peer reviewed, but should not be considered the official version of record. They are citable by the Digital Object Identifier (DOI®). "Just Accepted" is an optional service offered to authors. Therefore, the "Just Accepted" Web site may not include all articles that will be published in the journal. After a manuscript is technically edited and formatted, it will be removed from the "Just Accepted" Web site and published as an ASAP article. Note that technical editing may introduce minor changes to the manuscript text and/or graphics which could affect content, and all legal disclaimers and ethical guidelines that apply to the journal pertain. ACS cannot be held responsible for errors or consequences arising from the use of information contained in these "Just Accepted" manuscripts.

Quadruple Hydrogen Bonding Supramolecular Elastomers for Melt Extrusion Additive Manufacturing

Xi Chen,¹ Callie E. Zawaski,² Glenn A. Spiering,¹ Boer Liu,¹ Christina M. Orsino,¹ Robert B. Moore,¹ Christopher B. Williams,² and Timothy E. Long ^{1,*}

¹ Department of Chemistry, Macromolecules Innovation Institute (MII), Virginia Tech, Blacksburg, VA, 24061

² Department of Mechanical Engineering, Macromolecules Innovation Institute (MII), Virginia
Tech, Blacksburg, VA, 24061

*Email: telong@vt.edu

Keywords: Quadruple hydrogen bonding, supramolecular polymer, extrusion additive manufacturing, microphase separation, rheology, mechanical property

Abstract

This manuscript describes the versatility of highly-directional, noncovalent interactions, i.e., quadruple hydrogen bonding (QHB), to afford novel polyurea segmented supramolecular polymers for melt extrusion 3D printing processes. The molecular design of the polyurea elastomers features (1) flexible polyether segments and relatively weak urea hydrogen bonding sites in the soft segments to provide elasticity and toughness, and (2) strong ureido-cytosine (UCyt) QHB in the hard segment to impart enhanced mechanical integrity. The resulting polyureas were readily compression-molded into mechanically-robust, transparent, and creasable films. Optimization of polyurea composition offered a rare combination of high tensile strength (95 MPa), tensile elongation (788 % strain), and toughness (94 MJ m⁻³), which are superior to a commercially

available Ninjaflex® elastomer. The incorporation of QHB facilitated melt processability, where hydrogen bonding dissociation provided low viscosities at printing temperatures. During cooling, directional self-assembly of UCyt QHB facilitated the solidification process and contributed to part fidelity with the formation of a robust physical network. The printed objects displayed high layer fidelity, smooth surfaces, minimal warpage, and complex geometries. The presence of highly-directional QHB effectively diminished mechanical anisotropy, and the printed samples exhibited comparable Young's moduli along (x-y direction, 0°) and perpendicular to (z-direction, 90°) the layer direction. Remarkably, the printed samples exhibited ultimate tensile strains approaching 500% in the z-direction prior to failure, which was indicative of improved interlayer adhesion. Thus, this design paradigm, which is demonstrated for novel polyurea copolymers, suggests the potential of supramolecular polymers with enhanced mechanical performance, melt-processability, recyclability, and improved interlayer adhesion for melt extrusion additive manufacturing processes.

Introduction

Additive manufacturing (AM, commonly termed 3D printing) has received intense academic and industrial attention during the past decade. AM creates three-dimensional objects from a predetermined computer-aided (CAD) model in a layer-by-layer fashion, which offers designers tremendous flexibility in realizing objects with tailored geometric structures and well-defined features that are not achievable through traditional manufacturing processes. Additionally, AM enables the production of light-weight polymeric products by tailoring their mesostructures (e.g., latticed or cellular topologies), which minimizes material waste while maintaining appearance and function. The exciting potential of AM allows the versatile fabrication of

customer-specific products to address emerging needs, especially in the fields of consumer products, medical devices, infrastructure, aerospace, and transportation.^{4–6}

Extrusion AM is among the most widely used AM processes due to its low cost and simple setup compared to other advanced manufacturing processes. Fused deposition modeling (FDM), also termed fused filament fabrication (FFF), continues to dominate the commercial market of extrusion-based 3D printing processes. FDM is a fabrication process where continuous thermoplastic filaments are fed through a heating element to achieve a molten, semi-liquid state. Upon extrusion from the nozzle, the polymer melt is deposited on top of the previously solidified layers to afford a new layer (x-y direction) following a predefined trajectory. Continuous repetitions of this process increase the height (z-direction) of the structure until the completion of a 3D architecture. One of the biggest challenges that limits the reliability of FDM printed objects is mechanical anisotropy, where the mechanical strength across the printed layers (z-direction) is significantly lower than along the printed layers (x-y direction). Most commercially relevant FDMprocessed polymers, e.g., acrylonitrile-butadiene-styrene copolymers (ABS), rely solely on molecular diffusion as the interlayer bonding mechanism.^{7–11} Optimized FDM process parameters maintain the interface temperature above the glass transition temperature (T_o) for a characteristic amount of time to promote molecular diffusion and entanglement to occur across the interface. 9-12 This is typically accomplished by tuning printing parameters such as nozzle temperature, build environment temperature, and printing rate, so that each deposited layer induces localized remelting of the previous layer. However, most polymers for FDM possess $T_{\rm g}$'s well above room temperature, and thus the large thermal gradient between the polymer melt and the atmosphere accelerates the cooling process and shortens the time that the melt remains above T_g . Seppala etal. determined the temperature profiles of the extruded ABS welding zone using infrared imaging

and reported the cooling rate is approximately 100 °C/s under typical printing conditions, which allowed only ~ 1 s for the weld temperature to remain above $T_{\rm g}$. ¹³ Thus, the limited time provided for molecular diffusion and entanglement between each deposited layer results in weak interlayer bonding and compromised mechanical performance. Potential solutions such as thermal treatment and high energy radiation were widely reported in the literature, where the former decreases the cooling rate with additional thermal energy applied during or after printing to increase intermolecular diffusion, and the latter creates chemical crosslinks to enhance interlayer bonding.^{7,9,14–16} Despite their demonstrated efficacy in literature, these additional strategies often complicate the printing processes and increase production costs. Moreover, the introduction of covalent linkages induces irreversible structural change and reduces the potential for subsequent recycling. Another critical issue that impedes the development of extrusion 3D printing is the narrow library of suitable printing materials. Currently, ABS and poly (lactic acid) (PLA) continue to dominate the market. However, these commercially available polymers exhibit key disadvantages, e.g., ABS suffers from relatively low mechanical strength and PLA suffers from brittleness due to crystallinity. Although considerable work has investigated the coextrusion of these polymers to yield reinforced composites with enhanced mechanical properties. 17–20 less focus is directed towards designing new polymers that combine strength and flexibility for extrusion 3D printing.

The introduction of supramolecular building blocks to design novel polymers for FDM provides solutions for the above challenges. Noncovalent interactions, including hydrogen bonding $^{21-23}$, ionic interactions $^{24-26}$, host-guest interactions $^{27-29}$, metal-ligand interactions 30 , and π - π stacking 31,32 , contribute to the thermo-reversible properties of supramolecular polymers. These reversible characteristics enable melt-processability at elevated temperatures while serving

as physical crosslinks to afford mechanical integrity at service temperatures. Additionally, noncovalent interactions potentially serve as "molecular stickers" to improve interlayer adhesion. Despite the great potential of supramolecular polymers for extrusion printing, only recent academic efforts disclosed new supramolecular materials for FDM processes. Our research group utilized melt transesterification coupled with post-polymerization ion-exchange to afford sulfonated poly (ether ester) ionomers bearing monovalent or divalent counterions. Polymers with divalent counterions provided beneficial melt rheological profiles for FDM due to stronger ionic interactions compared to monovalent counterparts. Printing of these polymers generated an array of complex geometries for controlled release applications. ^{33,34} Recently, Ellson et al. reported the synthesis of thiourethane thermoplastics for FDM through step-growth polymerization of 2,20-(ethylenedioxy)diethanethiol (EDDT) and hexamethylene diisocyanate (HDI).³⁵ The presence of thermally-reversible hydrogen bonds facilitated processing at high temperatures and contributed to excellent mechanical toughness (up to 92 MJ m⁻³) in molded or printed parts. The resulting polymers exhibited enhanced mechanical isotropy with ultimate tensile strengths in the build direction (z-direction, 90°) reaching ~80 % relative to the printed direction (x-y direction, 0°).^{34,35} Despite these promising improvements, large variances in elongation in different directions remained in the printed parts. Maximum strains in the z-direction remained far below 10 % of those in the x-y printing direction, presumably due to the relatively weak physical interactions within the polymers.

Meijer *et al.* and Hailes *et al.* reported supramolecular polymers functionalized with quadruple hydrogen bonding (QHB) motifs of ureido-pyrimidinone (UPy)³⁶ and ureido-cytosine (UCyt)^{37,38} in their seminal work. These QHB units feature a complementary interaction with donor-donor-acceptor-acceptor (DDAA) arrays with high dimerization constants ($K_{dim} > 10^6 M^{-1}$

for UPy and $K_{dim} > 2.5 \times 10^5 \,\mathrm{M}^{-1}$ for UCyt in chloroform), which are several orders of magnitude stronger than single or dimeric hydrogen bond ($K_{dim} \le 10^2 \text{ M}^{-1}$). These strong noncovalent interactions render reinforcement of mechanical properties, leading to a broader service window and superior mechanical strength than polymers with single- or dimeric- hydrogen bonding sites.³⁹ ⁴² Moreover, OHB imparts "smart" properties to the polymer, including shape-memory and selfhealing, where its strong dimerization tendency enables efficient shape recovery and crack repair abilities. Yan et al. reported segmented supramolecular polymers containing UPy moieties in the hard segment. The damaged samples displayed nearly full recovery of their mechanical strength at room temperature after two days, which demonstrated potential applications for intelligent soft materials and flexible electronics. 15 Wei and coworkers designed a dynamic network consisting of poly(tetramethylene ether) glycol (PTMEG) and four-arm, star-shaped, poly(ε-caprolactone) (4PCL) precursors functionalized with UPy endgroups. 44 The polymer network exhibited a tripleshape memory behavior with the permanent shape defined by the strong UPy hydrogen bonding interactions. Moreover, intrinsic self-healing of the damaged sample was achieved upon heating the sample to 40 °C for 2 d because of the reassociation of the hydrogen bonds. Therefore, based on the high directionality, reversibility, and excellent intrinsic healing ability of QHB reported in the literature, the incorporation of QHB into polymers is anticipated to enable new materials for FDM with superior mechanical properties, excellent melt processability, and improved interlayer adhesion.

In the present work, facile one-pot step-growth polymerization utilizing a novel, bioinspired difunctional cytosine monomer synthesized UCyt-containing segmented polyureas. The soft segment consisted of flexible polyether chains and relatively weak urea bidentate hydrogen bonds to impart flexibility and toughness. The hard segment contained UCyt QHB to offer strong physically-crosslinked domains to support the mechanical integrity of the polymer. Thermal, thermomechanical, morphological, and rheological analysis revealed the influence of QHB on the physical properties, which served to predict the printability of the polymers. Printing above the hydrogen bonding dissociation temperatures minimized flow resistance during extrusion. In addition, re-association of hydrogen bonds during cooling enabled the polymer to rapidly recover mechanical strength and retain the as-deposited shape, which is essential for part fidelity. The FDM printed parts displayed high layer definition, smooth finish, minimal warpage, and low anisotropy. This work presents the identification of novel QHB-containing polymers, which demonstrates the potential of supramolecular polymers for future FDM.

Scheme 1. Synthesis of bis-cytosine monomer

$$+ 2.1 \text{ eq} \xrightarrow{\text{O} \text{N}} \xrightarrow{\text{NH}_2} \xrightarrow{\text{K}_2\text{CO}_3, \text{ DMSO}} \xrightarrow{\text{H}_2\text{N}} \xrightarrow{\text{N}} \xrightarrow{\text{N}$$

Scheme 2. One-pot step-growth polymerization of non-segmented (0 mol% hard segment, 0 PU) and segmented (20 and 40 mol% hard segment, 20 and 40 PU) polyureas

Results and Discussion

Monomer and polymer synthesis

Michael addition of cytosine to both ends of 1,4-butanediol diacrylate provided the novel bis-cytosine monomer, and a stoichiometric excess of cytosine was added to ensure a quantitative reaction conversion. The reaction occurred readily at room temperature in DMSO and was complete after 16 h. Unlike our previous mono-functionalized cytosine acrylate monomer that was soluble in a variety of organic solvents, ^{39,40} the bis-cytosine monomer only exhibited solubility in

DMSO. Purification of the bis-cytosine monomer was achieved simply through stirring the reaction mixture in water to precipitate the product and remove the excess reactants (cytosine and K₂CO₃). Subsequent filtration and drying afforded white solids with high yields of >95 %. ¹H and ¹³C nuclear magnetic resonance (NMR) spectra in Figure S1 and mass spectroscopy confirmed the chemical structure and purity of the product. The mild reaction conditions, simple purification procedures, and high monomer yields facilitated the large-scale synthesis of the monomer.

In the next step, facile one-pot step-growth polymerization allowed the preparation of nonsegmented and segmented polyureas (Scheme 2). For the non-segmented polyurea (0 PU), the reaction mixture remained clear in anhydrous DMF. Since the bis-cytosine monomer was insoluble in DMF, a DMSO/DMF cosolvent was employed for the synthesis of segmented polyureas (20 and 40 PU) to ensure the reaction proceeded in a homogeneous solution. During the polymerizations, both non-segmented and segmented polyurea reaction mixtures displayed a significant viscosity increase, which indicated the formation of urea and UCyt hydrogen bonding units. Compression-molding of the polyurea samples at 130 °C afforded optically-clear films with excellent mechanical robustness (Scheme 2). ¹H NMR spectroscopy (Figure S2) confirmed the polyurea structures and determined the hard segment content for each polymer, which closely aligned with the original feed ratios (0, 20, and 40 mol%). Characterization of the number-average molecular weight (M_n) and polydispersity (PDI) using gel permeation chromatography (GPC) was impossible as the polymers were difficult to elute from the column due to interactions between the polymer and the column. In addition, high physical crosslink densities resulted in strong molecular aggregation even at low concentrations (Figure S3), which also complicated molecular weight measurement. 45,46

Table 1. Summary of polyurea composition, thermal property, and mechanical properties

Polymer	Hard segment content ^a (mol%)	$T_{d,5wt\%}^{b}$ (°C)	Young's modulus'(MPa)	Tensile strength at break ^c (MPa)	Strain at break ^c (%)	Toughness ^c (MJ m ⁻³)
0 PU	0	329	73±2	21±2	856±28	99±4
20 PU	20	327	95±7	21±1	788±28	94±1
40 PU	40	308	106±3	19±2	604±44	69±9
20 PU-printed-0°	20	327	44±4	8±1	1185±169	81±13
20 PU-printed-90°	20	327	46±5	5±1	478±33	21±2

^a ¹H NMR, DMSO-*d*₆+CDCl₃, 23 °C

^c Tensile testing, 23 °C, 100 mm/min

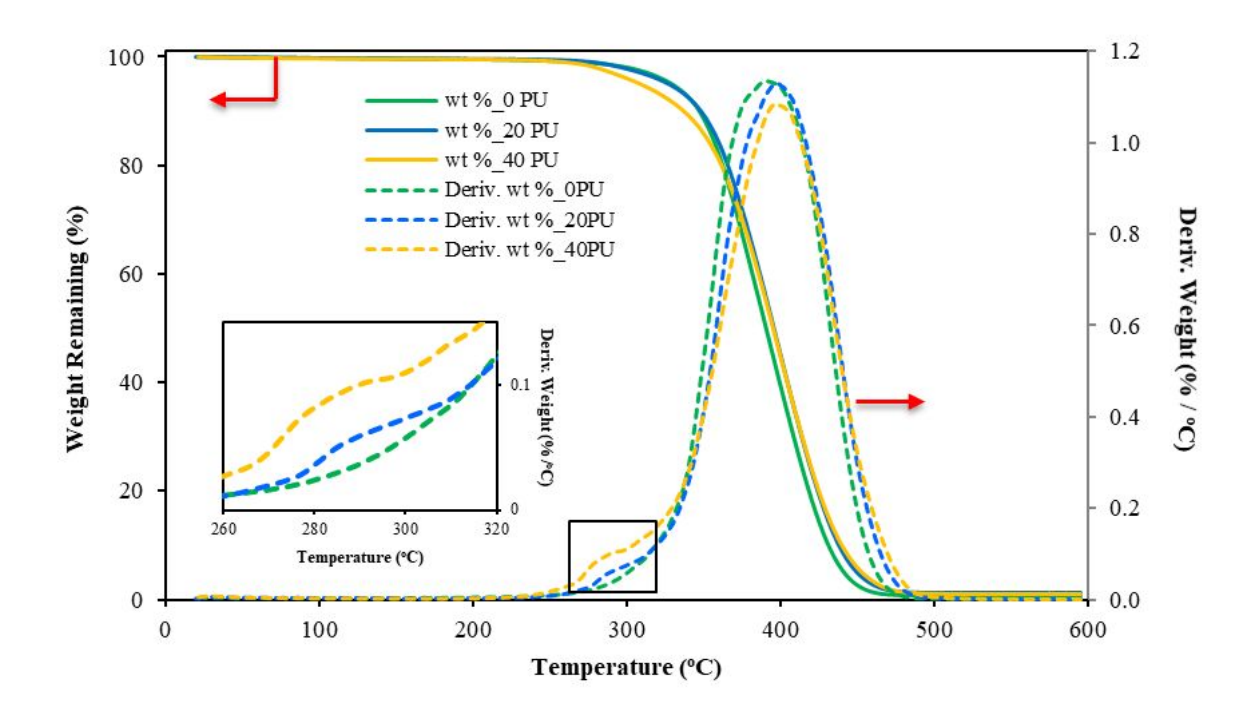


Figure 1. TGA thermograms of polyureas with varied hard segment content. TGA was performed from ambient to $600 \, ^{\circ}\text{C}$ at $10 \, ^{\circ}\text{C/min}$ under N_2 .

Investigation of physical properties and printability of the polyureas

Thermogravimetric analysis (TGA) profiles in Figure 1 reveal the thermal stability of polyureas with varied hard segment contents. $T_{d,5wt\%}$ is recognized as an indicator for polymer

^b TGA, 25-600 °C, 10 °C/min, N₂

degradation, which is near 329 °C for the non-segmented polyurea (0 PU). This is consistent with the thermal degradation temperatures of polyureas, which are typically between 300-400 °C.⁴⁷⁻⁴⁹ Increasing the hard segment content decreased the thermal stability of the polyureas (Table 1), as reflected by the appearance of a small shoulder (Figure 1 inset) in the derivative weight loss profiles between 280 °C to 300 °C for both the 20 and 40 PU prior to urea degradation. This is due to the lower thermal stability of the UCyt unit in the hard segment, where the degradation pathway involved the formation of cytosine and isocyanate (a reverse polymerization reaction).^{39,50,51}

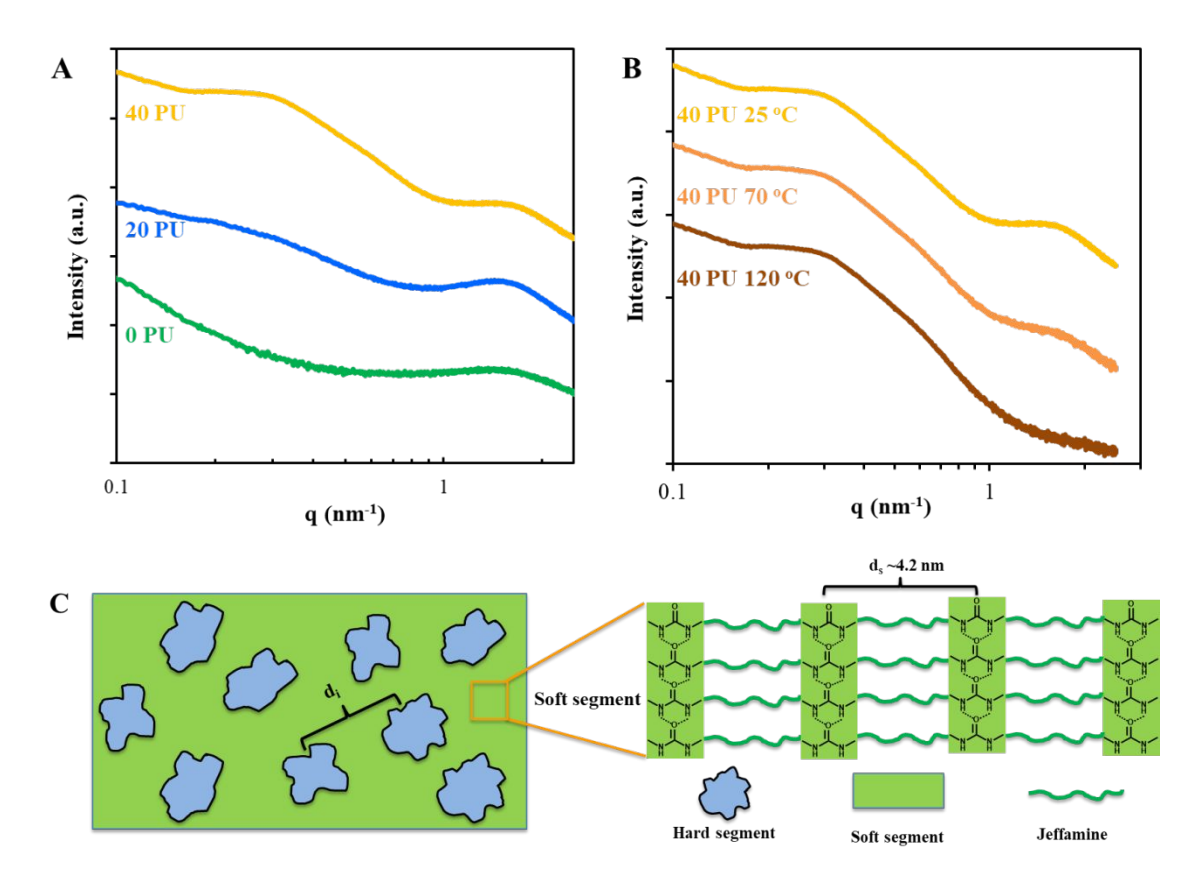


Figure 2. (A) SAXS of the polyureas samples with varied hard segment contents (B) SAXS profiles of the 40 PU at varied temperatures. The secondary ordering within the soft segment disappeared as the urea hydrogen bonding dissociates and (C) a schematic model of the polymer morphologies. The green and the blue regions represent the soft and the hard phase, respectively. The molecular representations on the right present the secondary structure within the soft phase, where the Jeffamine chains (curved green lines) are stacked together through the urea hydrogen bonds.

Small-angle X-ray scattering (SAXS) profiles in Figure 2A provide insights into bulk morphologies of the polyureas with different hard/soft compositions. At lower scattering vectors (q < 1 nm⁻¹), the 0 PU sample was featureless, indicating the absence of phase separation on a larger length scale due to its non-segmented structure. A broad scattering maximum started to emerge for the 20 PU sample at ~0.30 nm⁻¹, which suggested the onset of phase-separation of the hard domain within the soft polymer matrix. This scattering maximum became more prominent when the hard segment content further increased to 40 mol% due to a stronger propensity of microphase separation between soft and hard domains. At higher scattering vectors ($q > 1.0 \text{ nm}^{-1}$), a scattering maximum located at ~ 1.50 nm⁻¹ remained relatively consistent for all PU samples, which suggested a periodic distribution of secondary structures with an average domain spacing of $d_s \sim 4.2$ nm. This secondary ordering is presumably correlated with the self-assembly within the soft segment, where bidentate hydrogen bonding between urea motifs facilitated the packing of the Jeffamine polyether chain and led to the formation of the ordered polyether and urea domains (Figure 2C). To further investigate the origin of this secondary ordering, variable temperature SAXS experiments (Figure 2B) were used to probe the structural transition of the secondary morphologies from 25-120 °C. Increasing the temperature resulted in the disappearance of the scattering maximum of the secondary structure, when the dissociation of relatively weak urea hydrogen bonds disrupted the ordered secondary structures at the elevated temperatures.

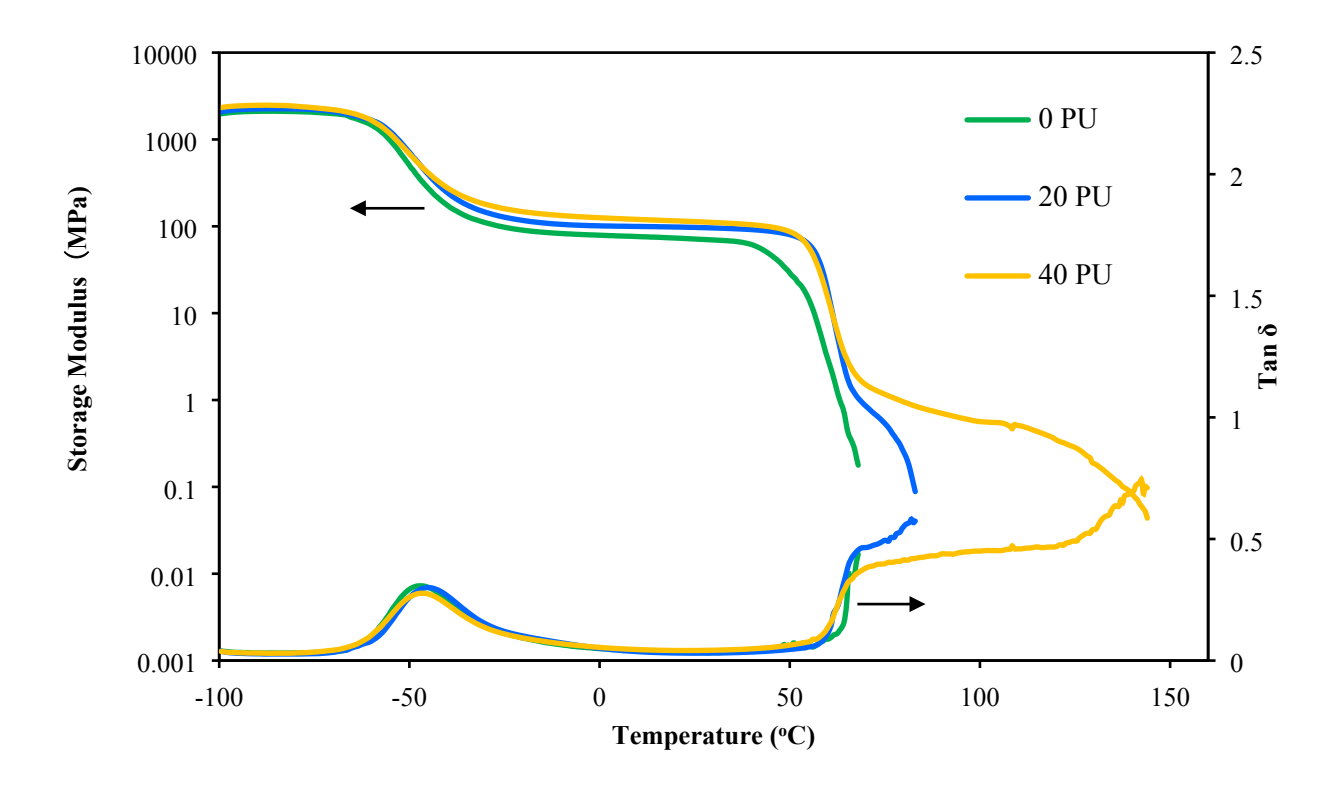


Figure 3. DMA profiles of polyureas with different hard segment incorporation. DMA was performed at 3 $^{\circ}$ C/min with an oscillatory amplitude of 15 μ m at 1 Hz

Dynamic mechanical analysis (DMA) (Figure 3) probed the influence of QHB on the thermomechanical performance of polyureas. The first storage modulus drop located near -50 °C originated from the long-range segmental relaxation of the soft segment. The corresponding $\tan \delta$ maxima indicated the $T_{\rm g}$ of the soft segment, whose locations remained relatively invariant with varied hard segment composition. Above soft segment $T_{\rm g}$, all samples exhibited a storage modulus plateau regime with the modulus increased with increasing hard segment incorporation. In this region, hydrogen bonding primarily served as physical crosslinks to offer structural integrity to the polymer until the second thermomechanical transition occurred at ~60 °C. The 0 PU failed to retain its mechanical strength and flowed at lower temperatures due to a relatively weak physical network within the polymer. Introducing the hard segment enhanced the thermomechanical resistance of

the polyureas. A short, secondary modulus plateau was observed for 20 PU near 70 °C, where the incorporation of QHB strengthened the physical network. This second plateau regime further extended to ~130 °C for 40 PU before gradually reaching the terminal flow state. The distinct viscoelastic performance of the PU series demonstrated the significant structural reinforcement of the polymers due to QHB within the hard segment, where complementary QHB between UCyt sites afforded a robust supramolecular network through inter- or intra-molecular crosslinking that prohibited chain unfolding and sliding upon thermomechanical stimuli.

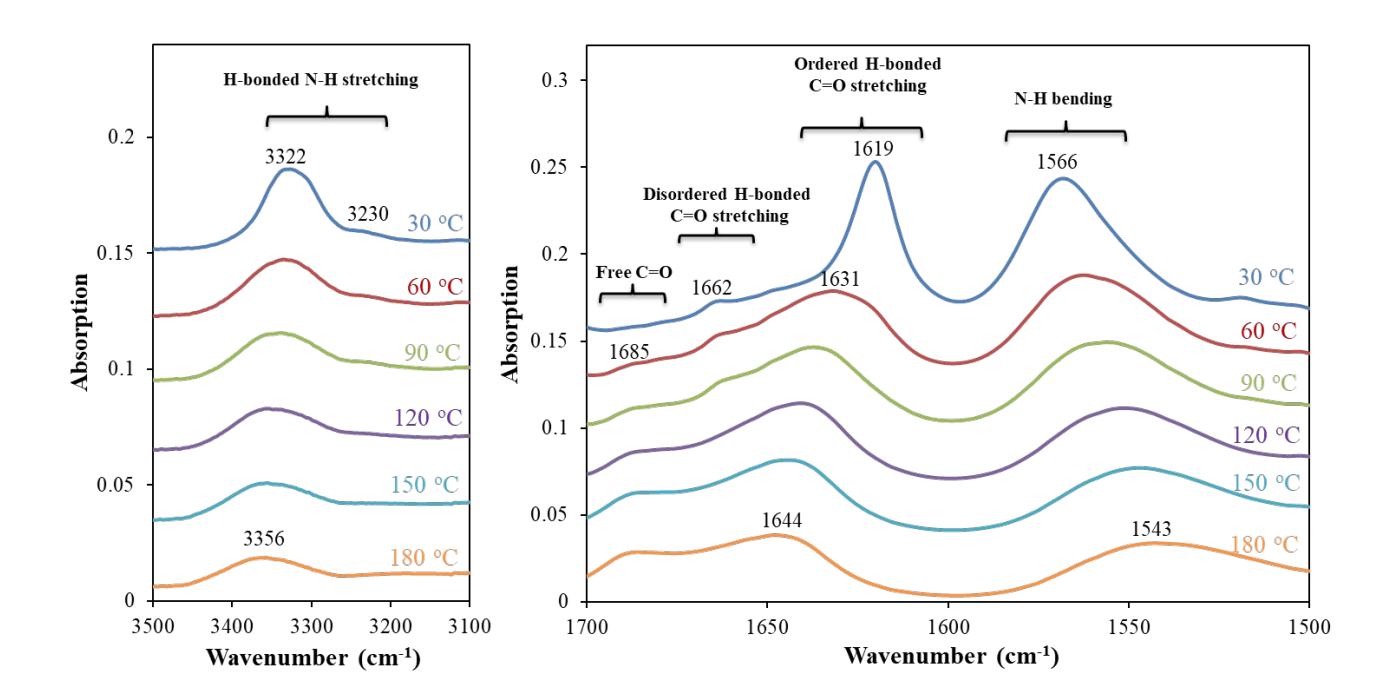


Figure 4. VT-FTIR spectra of 20 PU. VT-FTIR was performed from 30 °C to 180 °C with a 30 °C interval.

Variable temperature Fourier-transform infrared (VT-FTIR) spectroscopy on the 20 PU sample revealed the dynamic characteristics of hydrogen bonds in response to thermal stimuli. Figure 4 depicts the infrared spectra of 20 PU from 30 °C to 180 °C. The characteristic peaks at 3322 and 3230 cm⁻¹ at 30 °C were indicative of the stretching vibrations of N-H groups, which are

typical for hydrogen-bonded N-H.39,52-54 The peak at 3322 cm⁻¹ broadened and blue-shifted to higher wavenumbers with increasing temperature and reached 3356 cm⁻¹ at 180 °C when hydrogen bond dissociated and the N-H bond was strengthened. In addition, the characteristic stretching vibration of the C=O group was observed between 1700 cm⁻¹ – 1600 cm⁻¹. The spectra at 30 °C displayed a sharp peak at 1619 cm⁻¹ that corresponded to ordered H-bonded C=O stretching vibration. As the temperature increased, the contribution from the component located at 1619 cm⁻¹ dramatically decreased and was replaced by a new broad maximum located at 1631 cm⁻¹ at 60 °C. and the maximum was further shifted to 1644 cm⁻¹ at 180 °C due to the dissociation of hydrogen bonds at elevated temperatures. 52,55 The band located at 1662 cm⁻¹ (30 °C) is assigned to disordered hydrogen-bonded C=O, which gradually disappeared along with the appearance of a new band at 1685 cm⁻¹ due to the formation of the free C=O groups.^{52,55} Finally, below 1600 cm⁻¹ 1, the spectral maximum at 1566 cm⁻¹ at 30 °C correlated with the contribution of the in-plane bending of N-H vibration. The peak broadened and redshifted to lower frequencies as the temperature increased, where hydrogen bonds dissociation liberated the anchored N-H group to facilitate the bending vibration.^{39,40,55} The shifting values (Figure S4) were plotted against temperature to assist visualization of the trend of hydrogen bonding dissociation. The leveling of the shifting values near 150 °C indicated most of the hydrogen bonds were dissociated above 150 °C.

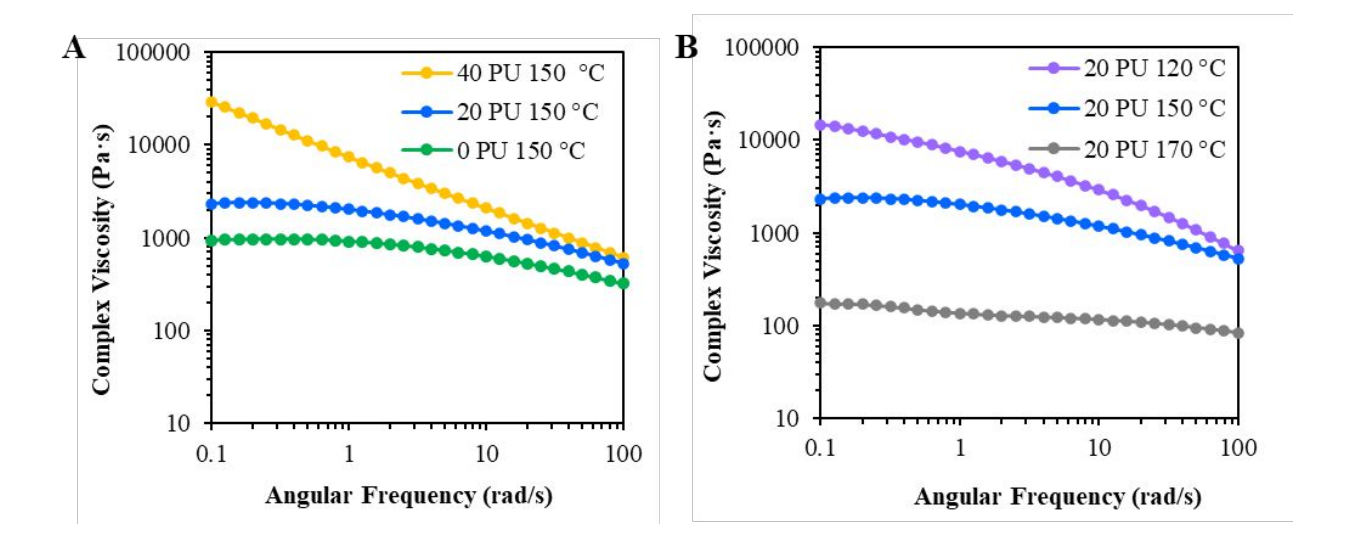


Figure 5. Melt viscosity of polyureas with increasing QHB contents at 150 °C (A) and 20 PU when cooling from 170 °C to 120 °C (B)

In an effort to evaluate the polyureas ability to be processed via FDM, rheological experiments were performed above the flow temperatures of the PU samples, as shown in Figure 5. Figure 5A depicts the melt viscosities of the PU samples with different hard segment contents at 150 °C. At a constant shear rate, the PU demonstrated, as expected, an increased viscosity with increasing hard segment incorporation, where complementary QHB in the hard domain afforded a robust physical network. Shear-thinning is advantageous for the FFF processes since it reduces flow resistance and facilitates melt extrusion from the nozzle. As shown in Figure 5A, increasing the hard segment content led to enhanced shear-thinning; moreover, the onset of the shear-thinning region shifted to a lower frequency as the hard segment increased. The 40 PU displayed a drastic linear decrease in melt viscosity with frequency throughout the testing regime, where mechanical deformation led to significant disruption of a highly physically-crosslinked network. In addition to shear-thinning, a second important criterion to assess a polymer printability is the ability to retain structural fidelity after extrusion from the printhead. ^{56–58} Therefore, rheological experiments probed melt viscosity of the 20 PU sample cooling from 170 °C to 120 °C (Figure 5B). The 20 PU

displayed a relatively flat viscosity profile with low viscosities of ~ 100 Pa·s at 170 °C due to the dissociation of most of the hydrogen bonds, as evidenced by the VT-FTIR data. Remarkably, decreasing the temperature to 120 °C led to a significant increase of viscosity by approximately two orders of magnitude, indicating restoration of mechanical integrity. Since the weak hydrogen bonds between the urea units were mostly dissociated at 120 °C (as evidenced by the variable-temperature SAXS data in Figure 2B), the formation of QHB crosslinked network is primarily responsible for the recovery of the melt mechanical integrity between 170 °C-120 °C. The advantageous rheological profiles in Figure 5B suggested 20 PU is an excellent candidate for FDM, as low viscosities at 170 °C would facilitate processing, while efficient restoration of mechanical properties during cooling would promote structural fidelity after extrusion.

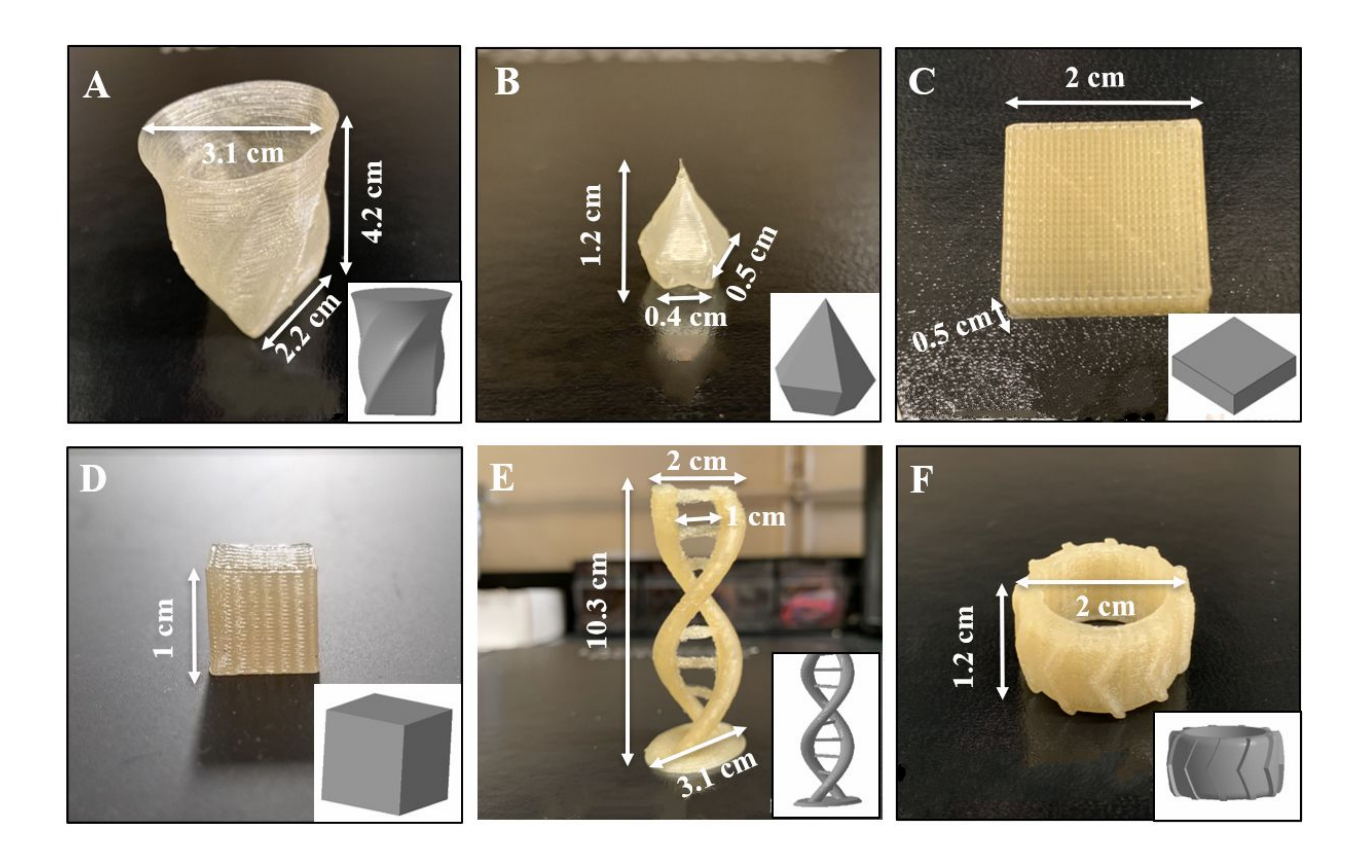


Figure 6. 3D Printed objects of 20 PU: (A) single-walled vase, (B) single-walled gem, (C) square, (D) cube, (E) DNA model, and (F) tire. The CAD models were laid next to the printed samples for comparison

Printing of the polyurea via FDM

Figure 6 depicts printed parts of 20 PU fabricated through FDM. The part fidelity of the sample was first evaluated through printing small single-walled (0 % material infill) objects such as a vase (Figure 6A) and a gem (Figure 6B). Since the single-walled objects feature small cross-sectional areas and thus required relatively short printing time for each layer, fast solidification of the polymer melt was crucial to achieving the desired structures. The resulting objects exhibited excellent structural resolution as reflected by clear road definitions, where rapid dimerization of QHB facilitated the solidification process. Interestingly, the printed single-walled objects remained intact and readily recovered to its original shape after repeated compressions (video S1), suggesting excellent ductility, toughness, and resilience. In addition to the single-walled parts, the fabrication of solid objects is another important approach to assess the printability of a material. Conventional semi-crystalline polymers suffer from undesirable curling effect due to unavoidable volume shrinkage during crystallization.³⁴ In our case, the squared (Figure 6C) and the cubed (Figure 6D) objects exhibited excellent part fidelity with minimal structural deformation and warpage. This is due to the low crystallinity of the polymer (as indicated by the WAXS data in Figure S5), which resulted in correspondingly low volume contraction during solidification. The outstanding printability of the polyurea highlighted the benefits of utilizing QHB-containing polymers for FDM, where strong physical crosslinks effectively achieved desired mechanical property in a short time while avoiding structural shrinkage. The excellent agreement between the final parts and CAD model (Figure 6E-F) demonstrated the capability of 20 PU to yield complex geometries such as a DNA double helix model and a tire. Noteworthy, high structural-resolution was achieved for the 3 cm (l) \times 2 cm (w) \times 10 cm (h) DNA object (Figure 6E), where the polymer

was surprisingly capable of spanning across a \sim 1 cm open gap without requiring any support material.

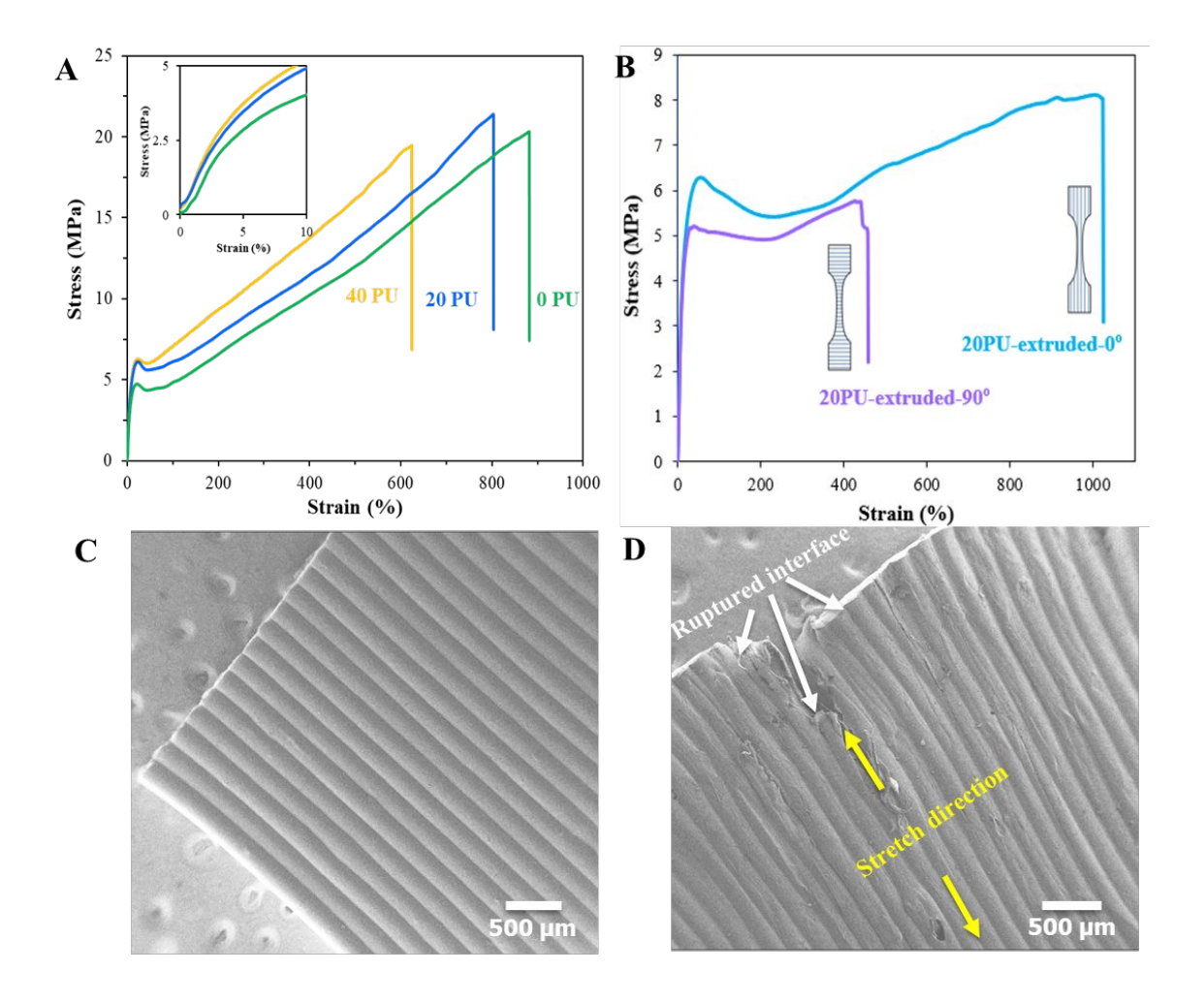


Figure 7. Tensile strength of (A) melt-pressed polyureas with varied quadruple hydrogen bonding incorporation (B) printed 20 PU sample bars along (0 $^{\circ}$) and perpendicular to (90 $^{\circ}$) the printing direction. SEM images of 0 $^{\circ}$ printed 20 PU sample bar (C) before tensile testing and (D) after tensile testing. The yellow arrows denote the tensile testing direction, and the white arrows indicate the ruptured sample interface after being stretched to > 1000 % strain. Strain rate: 100 mm/min

Tensile properties of the compression-molded and printed samples

Stress-strain profiles in Figure 7A present the tensile properties of the compression-molded samples at room temperature, summarized in Table 1. The tensile curves were characterized by a steep linear increase in stress at the elastic region, which was consistent with the high mechanical

strength of the polymers. Incorporation of the hard segment led to an increase in Young's modulus from 73 MPa to 106 MPa in this region, which closely aligned with the DMA data (Figure 3) at room temperature. The increase in mechanical strength indicated that OHB in the hard segment effectively prohibited the chain movement by serving as dense physical crosslinks to anchor the structure. At ~ 10% strain, the polyureas exhibited a well-defined yield point followed by a decrease in stress, when the physical network was partially disrupted to allow macromolecular chains to slide past one another.⁵⁹ As expected, the yield strength increased with increasing hard segment content, implying the introduction of QHB increased the energy barrier for plastic deformation. Further increasing the strain marked a cold-drawing region started at ~80 % strain, when the samples experienced a steady increase in stress as necking gradually propagated along the testing area until failure. The slope of strain hardening increased while the strain at break decreased with increasing hard segment content. Moreover, the toughness of the samples, which was determined by integrating the area under the stress-strain curve, decreased with increasing hard segment incorporation. The 0 PU sample exhibited an ultra-high toughness of 99 MJ m⁻³, where the urea hydrogen bonding sites within the soft matrix served as sacrificial bonds to facilitate energy dissipation during mechanical deformation. Yoshida et al. also observed a significant increase in the toughness of ABA block copolymers through incorporating sparse dynamic bonds in the central soft block of the polymers. 60 The optimal PU sample, i.e., 20 PU, demonstrated a rare combination of high modulus (95 MPa), elongation (788 %), and toughness (94 MJ m⁻³), which is superior to a commercially available FDM elastomer, Ninjaflex[®]. The latter only exhibits a modulus of 12 MPa and a tensile elongation of 660 %. The outstanding mechanical properties of the PU samples originate from the microphase-separated structure of the polyureas. Strong QHB units in the hard segment provided a robust physical network to impart mechanical strength, while

the highly flexible polyether chain and the weak urea hydrogen bonding sites in the soft segment collectively imparted excellent elasticity and toughness. The dynamic nature of hydrogen bonds afforded a repeated dissociation-association of the physical network during mechanical deformation, allowing for the progressive opening of the inter/intra-chain interactions to achieve high extensibility.⁴³ Simultaneously, the disrupted hydrogen bonds rapidly reassociated under strain to regenerate a transient network and retain the mechanical integrity of the polymer.^{43,61}

The tensile results of printed specimen in Figure 7B evaluated the mechanical anisotropy of the extruded 20 PU samples by comparing the tensile properties of printed dogbones with layer directions orthogonal (z-direction, 90°) and parallel (x-y direction, 0°) to the tensile direction. The samples that were tested in the 90 ° direction exhibited similar Young's modulus compared to the samples that were tested in the 0° direction (Table 1), indicating relatively isotropic mechanical strength (Table 1). The 0 ° samples demonstrated a higher elongation (1185 % strain) compared to the compression-molded film (~788 % strain), which is presumably attributed to a better structural alignment for the extruded sample along the tensile direction. 2D SAXS comparison between the extruded (Figure S7A) and compression-molded sample (Figure S7B) provided morphological evidence for the tensile data. The oval scattering rings at lower scattering-vectors revealed the long-range orientation for the 0 o extruded samples along the extrusion direction, where the oriented hard domains resided within the locally isotropic soft matrix. In contrast, the isotropic scattering features of the compression-molded sample (Figure S7B) indicated the randomly oriented morphologies throughout the polymer structure. The 90 ° printed samples surprisingly displayed a high strain-at-break of 478 %, which accounted for 40 % of the 0 ° printed samples and 60 % of the compression-molded films. This remarkable interlayer adhesion is significantly higher than the previously reported polymers with or without weak physical interactions, where

earlier 90 ° printed samples only displayed less than 10 % of the strain compared to the 0 ° printed sample.34,35,62-64 SEM imaging of a printed tensile bar shown in Figure 7C revealed smooth surface finish and excellent printing resolution, where the rapid formation of OHB-crosslinked network helped to retain the shape of the polymer melts to facilitate solidification. In addition, Figure 7C showed the roads were tightly fused together without voids or gaps in between, which suggested excellent layer adhesion. The low $T_{\rm g}$ polyether matrix promoted thermal diffusion of polymer chains across the printed layers, and the interlayer bonding was further strengthened by the association of highly-directional QHB. The SEM image of the ruptured 0 oprinted tensile bar after tensile testing in Figure 7D revealed the layers were still welded as a single piece despite stretching to >1000 % strain. This phenomenon is in stark contrast to the macroscopic phenomenon of many materials printed through FDM, where the layers disintegrated readily to separate roads as the cross-section of the sample was dramatically reduced during plastic deformation.³⁴ The exceptionally low mechanical anisotropy and high part fidelity of the printed samples further demonstrated that the synergy of strong multiple-hydrogen bonds with a flexible polymer matrix is beneficial for the extrusion 3D printing process.

Conclusion

In summary, supramolecular polymer design provided bio-inspired, QHB containing segmented polyurea thermoplastic elastomers for FDM processes. Facile one-pot step-growth polymerization enabled the preparation of a series of PUs with varied soft and hard segment contents, where the former consisted of flexible polyether chains and bidentate urea hydrogen bonding units, and the latter contained a short butyl chain with strong UCyt QHB moieties. Systematic characterizations of the polymers revealed that the incorporation of QHB enhanced the mechanical strength and extended the plateau modulus region by serving as a thermomechanically-robust physical network.

The polymers demonstrated high strength, extensibility, and toughness due to microphase-separated morphologies between the soft and hard segments. In addition, QHB significantly influenced the polymers rheological profiles, enabling melt-processability and facilitating the solidification step, which is beneficial to FDM. The resulting 3D printed objects featured superior layer definition, high part fidelity, minimal warpage, and complex geometries. Moreover, utilizing QHB supramolecular chemistry reinforced interlayer adhesion through strong "molecular stickers" to achieve stronger anchoring of the printed layers, which minimized mechanical anisotropy and circumvented a post-curing process. These results demonstrate the promise of QHB PU supramolecular polymers to impact the design and fabrication of future 3D printable materials with superior mechanical properties to enable customized objects with high printing quality.

Experimental

Materials

Cytosine, 1,4-butanediol diacrylate, and hexamethylene diisocyanate were purchased from TCI and used without further purification. Potassium carbonate (K_2CO_3 , Fisher Scientific) was used as received. Jeffamine[®] THF 100 (M_n =1000 g/mol) was obtained from Huntsman. Dimethyl sulfoxide (DMSO, anhydrous, HPLC), N, N-dimethylformamide (DMF, anhydrous, HPLC), and methanol (MeOH, HPLC) were purchased from Spectrum and used as received.

Analytical methods

Proton nuclear magnetic resonance (¹H NMR) spectroscopy was performed at 23 °C on an Agilent U4-DD2 400 Hz spectrometer to analyze the chemical structures of the monomers and the polymers. High-resolution TOF mass spectroscopy (HRMS) was conducted on an Agilent 6220 mass spectrometer with a TOF analyzer in positive ion mode. Dynamic light scattering (DLS) measurements were operated at 30 °C on a Malvern Zetasizer Nano Series using a 4 mW He–Ne

laser at a wavelength of 633 nm and an avalanche photodiode (APD) detector. The sample was measured at a concentration of 1.0 mg/mL in DMF. Thermogravimetric analysis (TGA) of the polymer samples was conducted utilizing a TA Instruments TGA Q500 under N₂ with a heating ramp from ambient temperature to 600 °C at 10 °C/min. The 5 wt % degradation temperature ($T_{\rm d,5}$ wt %) was utilized to indicate the polymers thermal stability. Dynamic mechanical analysis (DMA) study characterized the thermomechanical properties of the polymers and was performed utilizing a TA Instruments Q800 in tension mode at an oscillatory amplitude of 10 µm at 1 Hz. Rectangular sample films were equilibrated at -100 °C and isothermal for 3 min, length measured, and ramped from -100 °C to 150 °C at 3 °C/min. VT-FTIR was performed on a Varian 670-IR spectrometer equipped with a PIKE Technologies variable temperature GladiATRTM attachment (diamond crystal). The spectra were collected every 30 °C from 30 to 180 °C. Rheological frequency sweep of the polyurea samples was conducted using a TA Instruments Discovery Hybrid Rheometer-3, samples were placed between two 25 mm parallel aluminum plates and tested at a frequency range of 0.1-100 rad/s. Scanning electron microscopy (SEM) was performed on LEO (Zeiss) 1550 field-SEM at an accelerating voltage of 5 kV, a ~5 nm Pt was deposited on the sample surface using a Leica ACE600 sputter prior to analysis.

Small-angle X-ray scattering (SAXS) and wide-angle X-ray scattering (WAXS) experiments were performed using a Rigaku S-Max 3000 3 pinhole SAXS system, equipped with a rotating anode emitting X-ray with a wavelength of 0.154 nm (Cu Kα). The sample-to-detector distance was 1600 mm for SAXS and 110 mm for WAXS, and the q-range was calibrated using a silver behenate standard. Two-dimensional SAXS patterns were obtained using a 2D multiwire, proportional counting, gas-filled detector, with an exposure time of 2 h. Two-dimensional WAXS diffraction patterns were obtained using an image plate with an exposure time of 1 h. The SAXS

data were corrected for sample thickness, transmission, and background, and were put on an absolute scale by correction using a glassy carbon standard from the Advanced Photon Source (APS). The SAXS/WAXS profiles were vertically shifted to facilitate a comparison of peak positions. All the SAXS and WAXS data were analyzed using the SAXSGUI software package to obtain radially integrated SAXS and WAXS intensity versus the scattering vector q (SAXS) or 2θ (WAXS) respectively, where $q = (4\pi/\lambda)\sin(\theta)$, θ is one half of the scattering angle and λ is the X-ray wavelength. Using the equation $d = 2\pi/q$ enabled the calculation of the domain spacing of each sample, where q represents the first-order scattering vector.

An Instron 5500R universal testing instrument measured tensile properties of the compression-molded and the printed samples at a rate of 100 mm/min. Tensile analysis data represented an average of five specimens with a calculated standard deviation. The area under the stress-strain curve was utilized to determine the sample toughness. The compression-molded samples films were punched using the ASTM D-638-V cutter to create tensile specimens for testing. Characterization of tensile anisotropy of the printed samples was performed following a method described in the previous literature, where the x-y and z tensile specimens were punched from the printed pentagon prisms with a wall thickness of a single-printed road and no infill.

Synthesis of bis-cytosine monomer (Scheme 1)

1,4-butanediol diacrylate (5 g, 25.22 mmol, 1 eq.), cytosine (6.17 g, 55.49 mmol, 2.2 eq.), and K_2CO_3 (0.5 g, 3.62 mmol) were charged into a 250 mL, round-bottomed flask. 120 mL DMSO was added, and the suspension was stirred at 21 °C overnight to afford a clear and colorless solution. Then, the mixture was poured into 600 mL deionized water and the white precipitants were filtered, washed with water, and dried under vacuum at 70 °C overnight to obtain white solids. Yield: > 95 %. ¹H NMR in dmso- d_6 confirmed the monomer structure (Figure S1): 7.51 (d), 6.99 (d), 5.59 (d),

3.98 (t), 3.80 (t), 2.65 (t), 1.54 (m). Mass spectrometry (ESI+): calculated m/z = 420.1755, found m/z = 420.1827.

Synthesis of non-segmented (0 PU) and segmented (20 PU and 40 PU) polyureas (Scheme 2)

Jeffamine® THF 100 was dried under vacuum at 120 °C overnight to remove moisture prior to reaction. The synthesis of non-segmented polyurea (0 PU) is summarized below: Jeffamine® THF 100 (55 g, 0.055 mol), and anhydrous DMF were charged into a 500 mL, round-bottomed flask equipped with a magnetic stir bar. Hexamethylene diisocyanate (9.251 g, 0.055 mol) was then added dropwise into the solution. The reaction was stirred at 85 °C for 16 h. After that, the polymer was purified through precipitation into a MeOH/H₂O = 1:2 (v/v) mixture twice, followed by drying under vacuum at 80 °C for 24 h to afford non-segmented polyurea solids. In a typical segmented polyurea synthesis, Jeffamine® THF 100 (47.24 g, 0.047 mol) and bis-cytosine monomer (4.965 g, 0.012 mol) were dissolved in a 300 mL anhydrous DMSO/DMF mixture (3:1, v/v) at 85 °C. Once the solution turned homogeneous, hexamethylene diisocyanate (9.932 g, 0.059 mol) was added dropwise into the mixture and stirred for 16 h, followed by the identical purification and drying procedures. ¹H NMR (Figure S2) confirmed the structure of the non-segmented and segmented polyureas.

3D printing process

Polymer filaments were prepared using a desktop single-screw extruder (Filabot Ex2). The material was extruded at 130 °C onto a TeflonTM conveyor belt to generate flexible filament strands (Figure S6). The filament diameter was 1.5 ± 0.1 mm, where strands with a tolerance of approximately ± 0.05 mm were used for printing. Parts were printed on a custom delta printer using a modified open-source firmware (Marlin 2011) and an all-metal hot-end (E3D V6). The nozzle diameter was 0.4 mm. A customized thin tube was placed between the extruder gear and

the end of the heating element to prevent the filament buckling and to limit oozing. Parts were printed on painter's tape (3M multi-purpose painter's tape #2090) that stuck to a room-temperature glass bed with a fan for active cooling. The extrusion temperature was set to 170 °C, and parts were printed with speeds of 5-10 mm/sec without any support structures.

Supporting information

¹H and ¹³C NMR spectra of bis-cytosine monomer, ¹H NMR spectra of polyureas with 0-40 mol% hard segment (0-40 PU), size distribution of 40 PU in DMF, spectral shifting of the hydrogen-bonded groups *vs.* temperature, WAXS of PU samples, and 2D SAXS patterns of the extruded and compression-molded 20 PU.

Acknowledgments

The authors acknowledge Prof. Feng Lin and Zhengrui Xu for expertise and instrumentation for electron microscopy. This material is based upon work supported by the National Science Foundation under Grant No. DMR-1809291. The authors thank the insightful discussion with Philip J. Scott and Emily M. Wilts and the support from the Department of Chemistry, Macromolecules Innovation Institute (MII), and Nanoscale Characterization and Fabrication Laboratory (NCFL) at Virginia Tech.

Conflict of Interest

The authors declare no competing conflict of interest.

References

(1) Wohlers Report 2018: 3D Printing and Additive Manufacturing State of the Industry: Annual Worldwide Progress Report; Wohlers Associates, 2018.

- (2) Herzberger, J.; Sirrine, J. M.; Williams, C. B.; Long, T. E. Polymer Design for 3D Printing Elastomers: Recent Advances in Structure, Properties, and Printing. *Prog. Polym. Sci.* **2019**, *97*, 101144.
- (3) Gao, W.; Zhang, Y.; Ramanujan, D.; Ramani, K.; Chen, Y.; Williams, C. B.; Wang, C. C. L.; Shin, Y. C.; Zhang, S.; Zavattieri, P. D. The Status, Challenges, and Future of Additive Manufacturing in Engineering. *CAD Comput. Aided Des.* **2015**, *69*, 65–89.
- (4) Ngo, T. D.; Kashani, A.; Imbalzano, G.; Nguyen, K. T. Q.; Hui, D. Additive Manufacturing (3D Printing): A Review of Materials, Methods, Applications and Challenges. *Compos. Part B* **2018**, *143* (February), 172–196.
- (5) Pekkanen, A. M.; Mondschein, R. J.; Williams, C. B.; Long, T. E. 3D Printing Polymers with Supramolecular Functionality for Biological Applications. *Biomacromolecules* **2017**, *18* (9), 2669–2687.
- (6) Ligon, S. C.; Liska, R.; Stampfl, J.; Gurr, M.; Mülhaupt, R. Polymers for 3D Printing and Customized Additive Manufacturing. *Chem. Rev* **2017**, *117*, 10212–10290.
- (7) Shaffer, S.; Yang, K.; Vargas, J.; Di Prima, M. A.; Voit, W. On Reducing Anisotropy in 3D Printed Polymers via Ionizing Radiation. *Polymer (Guildf)*. **2014**, *55*, 5969–5979.
- (8) Aliheidari, N.; Christ, J.; Tripuraneni, R.; Nadimpalli, S.; Ameli, A. Interlayer Adhesion and Fracture Resistance of Polymers Printed through Melt Extrusion Additive Manufacturing Process. *Mater. Des.* **2018**, *156*, 351–361.
- (9) Kishore, V.; Ajinjeru, C.; Nycz, A.; Post, B.; Lindahl, J.; Kunc, V.; Duty, C. Infrared Preheating to Improve Interlayer Strength of Big Area Additive Manufacturing (BAAM) Components. *Addit. Manuf.* **2017**, *14*, 7–12.
- (10) Turner, B. N.; Strong, R.; Gold, S. A. A Review of Melt Extrusion Additive Manufacturing Processes: I . Process Design and Modeling. **2014**, *3* (March 2013), 192–204.
- (11) Sun, Q.; Rizvi, G. M.; Bellehumeur, C. T.; Gu, P. Effect of Processing Conditions on the Bonding Quality of FDM Polymer Filaments. *Rapid Prototyp. J.* **2008**, *14* (2), 72–80.
- (12) Seppala, J. E.; Hoon Han, S.; Hillgartner, K. E.; Davis, C. S.; Migler, K. B. Weld Formation during Material Extrusion Additive Manufacturing. *Soft Matter* **2017**, *13* (38), 6761–6769.
- (13) Seppala, J. E.; Migler, K. D. Infrared Thermography of Welding Zones Produced by Polymer Extrusion Additive Manufacturing. *Addit. Manuf.* **2016**, *12*, 71–76.
- (14) Hart, K. R.; Dunn, R. M.; Sietins, J. M.; Hofmeister Mock, C. M.; Mackay, M. E.; Wetzel, E. D. Increased Fracture Toughness of Additively Manufactured Amorphous Thermoplastics via Thermal Annealing. *Polymer (Guildf)*. **2018**, *144*, 192–204.
- (15) Ravoori, D.; Prajapati, H.; Talluru, V.; Adnan, A.; Jain, A. Nozzle-Integrated Pre-Deposition and Post-Deposition Heating of Previously Deposited Layers in Polymer Extrusion Based Additive Manufacturing. *Addit. Manuf.* **2019**, *28* (May), 719–726.

- (16) Wady, P.; Wasilewski, A.; Brock, L.; Edge, R.; Baidak, A.; McBride, C.; Leay, L.; Griffiths, A.; Vallés, C. Effect of Ionising Radiation on the Mechanical and Structural Properties of 3D Printed Plastics. *Addit. Manuf.* 2020, 31 (April 2019), 100907.
- (17) Brenken, B.; Barocio, E.; Favaloro, A.; Kunc, V.; Pipes, R. B. Fused Filament Fabrication of Fiber-Reinforced Polymers: A Review. *Addit. Manuf.* **2018**, *21* (October 2017), 1–16.
- (18) Jiang, D.; Smith, D. E. Anisotropic Mechanical Properties of Oriented Carbon Fiber Filled Polymer Composites Produced with Fused Filament Fabrication. *Addit. Manuf.* **2017**, *18*, 84–94.
- (19) Turner, B. N.; Gold, S. A. A Review of Melt Extrusion Additive Manufacturing Processes: II. Materials, Dimensional Accuracy, and Surface Roughness. **2015**, *3* (February 2013), 250–261.
- (20) Shofner, M. L.; Lozano, K.; Rodríguez-Macías, F. J.; Barrera, E. V. Nanofiber-Reinforced Polymers Prepared by Fused Deposition Modeling. *J. Appl. Polym. Sci.* **2003**, *89* (11), 3081–3090.
- (21) Author, H. B.; Sijbesma, R. P.; Beijer, F. H.; Brunsveld, L.; Folmer, B. J. B.; Hirschberg, J. J. K. K.; Lange, R. F. M.; Lowe, J. K. L.; Meijer, E. W. Reversible Polymers Formed from Self-Complementary Monomers Using Quadruple. *Source Sci. New Ser.* **1997**, *278* (5343), 1601–1604.
- (22) Sivakova, S.; Rowan, S. J. Nucleobases as Supramolecular Motifs. *Chem. Soc. Rev.* **2005**, 34 (1), 9–21.
- (23) Lafitte, V. G. H.; Aliev, A. E.; Horton, P. N.; Hursthouse, M. B.; Bala, K.; Golding, P.; Hailes, H. C. Quadruply Hydrogen Bonded Cytosine Modules for Supramolecular Applications. *J. Am. Chem. Soc.* **2006**, *128* (20), 6544–6545.
- (24) Bara, J. E.; Finotello, A.; Magee, J. W.; Qian, S.; O'Harra, K. E.; Dennis, G. P.; Noble, R. D. 110th Anniversary: Properties of Imidazolium-Based Ionic Liquids Bearing Both Benzylic and n-Alkyl Substituents. *Ind. Eng. Chem. Res.* **2019**, *58* (38), 17956–17964.
- (25) Chen, X.; Talley, S. J.; Haag, J. V.; Spiering, G. A.; Liu, B.; Drummey, K. J.; Murayama, M.; Moore, R. B.; Long, T. E. Doubly Charged ABA Triblock Copolymers: Thermomechanically Robust Physical Network and Hierarchical Microstructures. *Macromolecules* **2019**, *52*, 9168–9176.
- (26) Lu, X.; Steckle, W. P.; Weiss, R. A. Ionic Aggregation in a Block Copolymer Ionomer. *Macromolecules* **1993**, *26* (22), 5876–5884.
- (27) Yan, X.; Cook, T. R.; Pollock, J. B.; Wei, P.; Zhang, Y.; Yu, Y.; Huang, F.; Stang, P. J. Responsive Supramolecular Polymer Metallogel Constructed by Orthogonal Coordination-Driven Self-Assembly and Host/Guest Interactions. *J. Am. Chem. Soc.* **2014**, *136* (12), 4460–4463.
- (28) Jones, J. W.; Zakharov, L. N.; Rheingold, A. L.; Gibson, H. W. Cooperative Host/Guest Interactions via Counterion Assisted Chelation: Pseudorotaxanes from Supramolecular Cryptands. *J. Am. Chem. Soc.* **2002**, *124* (45), 13378–13379.

- (29) Besenius, P. Controlling Supramolecular Polymerization through Multicomponent Self-Assembly. *J. Polym. Sci. Part A Polym. Chem.* **2017**, *55* (1), 34–78.
- (30) Burnworth, M.; Tang, L.; Kumpfer, J. R.; Duncan, A. J.; Beyer, F. L.; Fiore, G. L.; Rowan, S. J.; Weder, C. Optically Healable Supramolecular Polymers. *Nature* **2011**, *472* (7343), 334–337.
- (31) Burattini, S.; Colquhoun, H. M.; Fox, J. D.; Friedmann, D.; Greenland, B. W.; Harris, P. J. F.; Hayes, W.; MacKay, M. E.; Rowan, S. J. A Self-Repairing, Supramolecular Polymer System: Healability as a Consequence of Donor-Acceptor π-π Stacking Interactions. *Chem. Commun.* 2009, No. 44, 6717–6719.
- (32) Burattini, S.; Greenland, B. W.; Hayes, W.; MacKay, M. E.; Rowan, S. J.; Colquhoun, H. M. A Supramolecular Polymer Based on Tweezer-Type Π-π Stacking Interactions: Molecular Design for Healability and Enhanced Toughness. *Chem. Mater.* **2011**, *23* (1), 6–8.
- (33) Pekkanen, A. M.; Zawaski, C.; Stevenson, A.; Dickerman, R.; Whittington, A. R.; Williams, C. B.; Long, T. E. Poly(Ether Ester) Ionomers as Water-Soluble Polymers for Material Extrusion Additive Manufacturing Processes. *ACS Appl. Mater. Interfaces* **2017**, *9*, 12324–12331.
- (34) Zawaski, C. E.; Wilts, E. M.; Chatham, C. A.; Stevenson, A. T.; Pekkanen, A. M.; Li, C.; Tian, Z.; Whittington, A. R.; Long, T. E.; Williams, C. B. Tuning the Material Properties of a Water-Soluble Ionic Polymer Using Different Counterions for Material Extrusion Additive Manufacturing. *Polymer (Guildf)*. 2019, 176 (June), 283–292.
- (35) Ellson, G.; Carrier, X.; Walton, J.; Mahmood, S. F.; Yang, K.; Salazar, J.; Voit, W. E. Tough Thiourethane Thermoplastics for Fused Filament Fabrication. *J. Appl. Polym. Sci.* **2018**, *45574*, 1–7.
- (36) Beijer, F. H.; Sijbesma, R. P.; Kooijman, H.; Spek, A. L.; Meijer, E. W. Strong Dimerization of Ureidopyrimidones via Quadruple Hydrogen Bonding. *J. Am. Chem. Soc.* **1998**, *120*, 6761–6769.
- (37) Lafitte, V. G. H.; Aliev, A. E.; Horton, P. N.; Hursthouse, M. B.; Bala, K.; Golding, P.; Hailes, H. C. Quadruply Hydrogen Bonded Cytosine Modules for Supramolecular Applications. *J. Am. Chem. Soc.* **2006**, *128* (20), 6544–6545.
- (38) Greco, E.; Aliev, A. E.; Lafitte, V. G. H.; Bala, K.; Duncan, D.; Pilon, L.; Golding, P.; Hailes, H. C. Cytosine Modules in Quadruple Hydrogen Bonded Arrays. *New J. Chem. This J. is c R. Soc. Chem. Cent. Natl. la Rech. Sci.* **2634**, *34*, 2634–2642.
- (39) Chen, X.; Zhang, K.; Talley, S. J.; Orsino, C. M.; Moore, R. B.; Long, T. E. Quadruple Hydrogen Bonding Containing Supramolecular Thermoplastic Elastomers: Mechanical and Morphological Correlations. *J. Polym. Sci. Part A Polym. Chem.* **2019**, *57* (1), 13–23.
- (40) Zhang, K.; Chen, M.; Drummey, K. J.; Talley, S. J.; Anderson, L. J.; Moore, R. B.; Long, T. E. Ureido Cytosine and Cytosine-Containing Acrylic Copolymers. *Polym. Chem.* 2016, 7, 6671–6681.
- (41) Song, Y.; Liu, Y.; Qi, T.; Li, G. L. Towards Dynamic but Supertough Healable Polymers

- through Biomimetic Hierarchical Hydrogen-Bonding Interactions. *Angew. Chemie Int. Ed.* **2018**, 13838–13842.
- (42) Guo, M.; Pitet, L. M.; Wyss, H. M.; Vos, M.; Dankers, P. Y. W.; Meijer, E. W. Tough Stimuli-Responsive Supramolecular Hydrogels with Hydrogen-Bonding Network Junctions. *J. Am. Chem. Soc.* **2014**, *136*, 6969–6977.
- (43) Yan, X.; Liu, Z.; Zhang, Q.; Lopez, J.; Wang, H.; Wu, H. C.; Niu, S.; Yan, H.; Wang, S.; Lei, T.; Li, J.; Qi, D.; Huang, P.; Huang, J.; Zhang, Y.; Wang, Y.; Li, G.; Tok, J. B. H., Chen, X.; Bao, Z. Quadruple H-Bonding Cross-Linked Supramolecular Polymeric Materials as Substrates for Stretchable, Antitearing, and Self-Healable Thin Film Electrodes. *J. Am. Chem. Soc.* **2018**, *140* (15), 5280–5289.
- Wei, M.; Zhan, M.; Yu, D.; Xie, H.; He, M.; Yang, K.; Wang, Y. Novel Poly(Tetramethylene Ether)Glycol and Poly(ε-Caprolactone) Based Dynamic Network via Quadruple Hydrogen Bonding with Triple-Shape Effect and Self-Healing Capacity. *ACS Appl. Mater. Interfaces* **2015**, *7*, 2585–2596.
- (45) Deng, G.; Cavicchi, K. A. Tuning the Viscoelastic Properties of Poly(n-Butyl Acrylate) Ionomer Networks through the Use of Ion-Pair Comonomers. *Macromolecules* **2017**, *50* (23), 9473–9481.
- (46) Green, M. D.; Long, T. E. Designing Imidazole-Based Ionic Liquids and Ionic Liquid Monomers for Emerging Technologies. *Polym. Rev.* **2009**, *49* (4), 291–314.
- (47) Montaudo, G. C. "Thermal Degradation Mechanisms in Condensation Polymers" in Developments in Polymer DegradationThermal Degradation Mechanisms in Condensation Polymers; N., G., Ed.; Springer, Dordrecht: London, 1987.
- (48) Dennis, J. M.; Steinberg, L. I.; Pekkanen, A. M.; Maiz, J.; Hegde, M.; Müller, A. J.; Long, T. E. Synthesis and Characterization of Isocyanate-Free Polyureas. *Green Chem.* **2017**, *20*, 243–249.
- (49) Lee, T. S.; Kim, D. Y.; Jiang, X. L.; Li, L.; Kumar, J.; Tripathy, S. Synthesis and Optical Properties of Polyureas with Azoaromatic Groups in the Main Chain. *Macromol. Chem. Phys.* **1997**, *198* (7), 2279–2289.
- (50) Caruso, S.; Foti, S.; Maravigna, P.; Montaudo, G. Mass Spectral Characterization of Polymers. Primary Thermal Fragmentation Processes in Polyureas. *J. Polym. Sci., Part A Polym. Chem. Ed.* **1982**, *20*, 1685–1696.
- (51) Montaudo, G.; Vitalini, D. The Effect of Ammonium Polyphosphate on the Mechanism of Thermal Degradation of Polyureas. *J. Polym. Sci., Part A Polym. Chem. Ed.* **1983**, *21*, 3321–3331.
- (52) Cheng, C.-C.; Chang, F.-C.; Wang, J.-H.; Chu, Y.-L.; Wang, Y.-S.; Lee, D.-J.; Chuang, W.-T.; Xin, Z. Large-Scale Production of Ureido-Cytosine Based Supramolecular Polymers with Well-Controlled Hierarchical Nanostructures. *RSC Adv.* **2015**, *5*, 76451–76457.
- (53) Coleman, M. M.; Lee, K. H.; Skrovanek, J. D.; Painter, C. P. Hydrogen Bonding in Polymers. 4. Infrared Temperature Studies of a Simple Polyurethane. *Macromolecules*

- , 19 (8), 2149–2157.
- (54) Yuan, Q.; Zhou, T.; Li, L.; Zhang, J.; Liu, X.; Ke, X.; Zhang, A. Hydrogen Bond Breaking of TPU upon Heating: Understanding from the Viewpoints of Molecular Movements and Enthalpy. *RSC Adv.* **2015**, *5*, 31153–31165.
- (55) Luo, N.; Wang, D. N.; Ying, S. K. Hydrogen-Bonding Properties of Segmented Polyether Poly(Urethane Urea) Copolymer. *Macromolecules* **1997**, *30* (15), 4405–4409.
- (56) Duty, C.; Ajinjeru, C.; Kishore, V.; Compton, B.; Hmeidat, N.; Chen, X.; Liu, P., Hassen, A. A.; Lindahl, J.; Kunc, V. A Viscoelastic Model for Evaluating Extrusion-Based Print Conditions. *Solid Free. Fabr. Symp. Proc.* **2017**, 495–506.
- (57) Liu, W.; Heinrich, M. A.; Zhou, Y.; Akpek, A.; Hu, N.; Liu, X.; Guan, X.; Zhong, Z.; Jin, X.; Khademhosseini, A.; Zhang, Y. S. Extrusion Bioprinting of Shear-Thinning Gelatin Methacryloyl Bioinks. Adv. Healthc. Mater. 2017, 6 (12), 1–11.
- (58) Ouyang, L.; Highley, C. B.; Rodell, C. B.; Sun, W.; Burdick, J. A. 3D Printing of Shear-Thinning Hyaluronic Acid Hydrogels with Secondary Cross-Linking. *ACS Biomater. Sci. Eng.* **2016**, *2* (10), 1743–1751.
- (59) Wang, S. Q.; Ravindranath, S.; Wang, Y.; Boukany, P. New Theoretical Considerations in Polymer Rheology: Elastic Breakdown of Chain Entanglement Network. *J. Chem. Phys.* **2007**, *127* (6), 064903.
- (60) Yoshida, S.; Ejima, H.; Yoshie, N. Tough Elastomers with Superior Self-Recoverability Induced by Bioinspired Multiphase Design. *Adv. Funct. Mater.* **2017**, *27* (30), 1–9.
- (61) Kushner, A. M.; Vossler, J. D.; Williams, G. A.; Guan, Z. A Biomimetic Modular Polymer with Tough and Adaptive Properties Synthesis of Biomimetic Linear Modular Polymer. *J. Am. Chem. Soc.* **2009**, *131*, 8766–8768.
- (62) de León, A. S.; Domínguez-Calvo, A.; Molina, S. I. Materials with Enhanced Adhesive Properties Based on Acrylonitrile-Butadiene-Styrene (ABS)/Thermoplastic Polyurethane (TPU) Blends for Fused Filament Fabrication (FFF). *Mater. Des.* **2019**, *182*, 108044.
- (63) Arif, M. F.; Kumar, S.; Varadarajan, K. M.; Cantwell, W. J. Performance of Biocompatible PEEK Processed by Fused Deposition Additive Manufacturing. *Mater. Des.* **2018**, *146*, 249–259.
- (64) Dolzyk, G.; Jung, S. Tensile and Fatigue Analysis of 3D-Printed Polyethylene Terephthalate Glycol. *J. Fail. Anal. Prev.* **2019**, *19* (2), 511–518.

For Table of Contents Use Only

